

# 1 Eruptive shearing of tube pumice: pure and simple

2  
3 D.B. Dingwell<sup>1</sup>, Y. Lavallée<sup>2</sup>, K.-U. Hess<sup>1</sup>, A. Flaws<sup>1</sup>, J. Marti<sup>3</sup>, A. R. L. Nichols<sup>4</sup>,  
4 H.A. Gilg<sup>5</sup>, B. Schillinger<sup>6</sup>

5  
6 <sup>1</sup> Earth and Environmental Sciences, Ludwig-Maximilians-Universität, Theresienstr. 41/III,  
7 80333 München, Germany

8 <sup>2</sup> Earth, Ocean and Ecological Sciences, University of Liverpool, United Kingdom

9 <sup>3</sup> Consejo Superior de Investigaciones Científicas, Institute of Earth Sciences Jaume Almera,  
10 Barcelona, Spain.

11 <sup>4</sup> Research and Development Center for Ocean Drilling Science, Japan Agency for Marine  
12 Earth Science and Technology (JAMSTEC), 2-15 Natsushima-cho, Yokosuka, Kanagawa  
13 237-0061, Japan.

14 <sup>5</sup> Ingenieursfakultät Bau Geo Umwelt, Technische Universität München, München, Germany

15 <sup>6</sup> Forschungsreaktor FRM-II, Technische Universität München, Garching, Germany

16  
17 Correspondence to: Y. Lavallée (ylava@liv.ac.uk)

## 18 19 **Abstract**

20 Understanding the physico-chemical conditions <sup>1</sup> extant and mechanisms operative during  
21 explosive volcanism is essential for reliable forecasting and mitigation of volcanic events.  
22 Rhyolitic pumices reflect highly vesiculated magma whose bubbles can serve as a strain  
23 indicator for inferring the state of stress operative immediately prior to eruptive  
24 fragmentation. Obtaining the full kinematic picture reflected in bubble population geometry  
25 has been extremely difficult, involving dissection of a small number of delicate samples. The  
26 advent of reliable high-resolution tomography has changed this situation radically. Here we  
27 demonstrate via the use of tomography how a statistically powerful picture of the shapes and  
28 connectivity of thousands of individual bubbles within a single sample of tube pumice  
29 emerges. The strain record of tube pumice is dominated by simple shear (not pure shear) in  
30 the late deformational history of vesicular magma before eruption. This constraint in turn  
31 implies that magma ascent is conditioned by a velocity gradient at the point of origin of tube  
32 pumice. Magma ascent accompanied by simple shear should enhance high eruption rates  
33 inferred independently for these highly viscous systems.

# Summary of Comments on Dingwell\_TubePumice\_SE\_v3x

---

Page: 1

---

 Number: 1 Author: Subject: Comment on Text Date: 10/Nov/2015 16:13:41  
Is this necessary?

## 34 **1 Introduction**

35           Upon nucleation, bubbles may grow, deform (stretch/collapse), coalesce and burst  
36 (Proussevitch and Sahagian, 1998; Proussevitch et al., 1993). This spectrum of behaviour  
37 expresses the variable state of stress in the magma column (Rust et al., 2003), and controls  
38 the evolution of the permeable porous network (Ashwell et al., 2015; Caricchi et al., 2011;  
39 Kendrick et al., 2013; Lavallée et al., 2013; Okumura et al., 2008; Pistone et al., 2012; Rust  
40 and Cashman, 2004; Wright et al., 2006; Wright and Weinberg, 2009), which regulates  
41 degassing, and thus internal pressure build-up required for fragmentation (Rust and Cashman,  
42 2011; Sahagian, 1999). Detail of the porous network in volcanic conduits is conventionally  
43 inferred from the characteristics of explosive eruptive products frozen-in upon fragmentation  
44 at the glass transition. This information has enabled the elaboration of elegant, magma ascent  
45 models, including mechanical strain simulations (Neuberg et al., 2006; Papale, 1999),  
46 permeable, porous network models (Collinson and Neuberg, 2012; Klug and Cashman, 1996)  
47 and fragmentation criteria (Koyaguchi et al., 2008; Spieler et al., 2004). Of all volcanic  
48 products, tube pumices (also termed fibrous or woody pumices) display one of the most  
49 spectacular, porous network configurations (e.g., Wright et al., 2006). Their enigmatic  
50 structure is made up of a collated amalgamation of elongate bubbles separated by extremely  
51 thin glassy walls. In fact, the remarkably delicate structure of tube pumices questions our  
52 understanding of the kinetics underlying volcanic eruptions at the point of fragmentation of  
53 such particular bubble-rich magmas.

54

55           Tube pumices have been postulated to offer a unique strain marker of the ductile-  
56 brittle processes enacted at fragmentation (Marti et al., 1999). Yet, the dilemma posed by  
57 tube pumices is that of stress and strain distribution inside volcanic conduits (Fig. 1).  
58 Fundamentally, do pores stretch due to pure shear or simple shear? Such contrasting strain

This page contains no comments

59 mechanistics may underline equally contrasting magma ascent dynamics. For instance, pure  
60 shear may be favoured in a regime where the strain induced by magma ascent acceleration  
61 exceeds the bubble growth rate associated by volatile exsolution (Mader et al., 1996).  
62 Alternatively, simple shear may be favoured in a regime where velocity gradient in areas of  
63 strain localisation along the conduit margin may stretch bubbles (Polacci, 2005). Thus the  
64 mechanisms causing tube pumice hold key tensorial information necessary to assess conduit  
65 flow mechanics. To resolve this dispute, we employ capabilities recently gained through  
66 advances in neutron computed tomography to reconstruct the porous network of tube pumice  
67 in unprecedented detail.

68

## 69 **2 Tube pumice of the Ramadas Volcanic Centre**

70 The Ramadas Volcanic Complex (RVC) is located in the Altiplano-Puna Plateau of  
71 the Central Andes, in NW of Argentina (Casas et al., 1995; Gauthier et al., 1994; Marti et al.,  
72 1999; Tait et al., 2009; Viramonte et al., 1984), near the township of San Antonio de los  
73 Cobres (Fig. 2a). Formed 8.7 Ma ago, the RVC is composed of a 4 x 3 km amphitheatre  
74 defined by the remains of rhyolitic domes and proximal pyroclastic deposits, set within  
75 uplifted Precambrian–Lower Cambrian meta-sedimentary rocks of the Puncoviscana  
76 Formation, and a widespread sequence of pyroclastic deposits mostly emplaced to the east  
77 from that vent area. Due to a lack of clear and continuous exposure, the vent boundaries are  
78 largely inferred from facies relationships (Tait et al., 2009; Viramonte et al., 1984) and  
79 geophysical gravimetric modelling (Casas et al., 1995).

80

81 Recent studies suggest that the Ramadas pyroclastic deposits were produced during an  
82 extremely explosive, Plinian scale eruption from a flaring point source vent structure (Tait et  
83 al., 2009). The RVC has erupted a complex suite of rhyolitic pyroclastic and coherent

 Number: 1 Author: Subject: Comment on Text Date: 27/Nov/2015 08:57:55

---

I think the authors should cite here:

Bouvet de Maisonneuve, C., O. Bachmann, and A. Burgisser, 2008, Characterization of juvenile pyroclasts from the Kos Plateau Tuff (Aegean Arc): insights into the eruptive dynamics of a large rhyolitic eruption: Bulletin of volcanology, v. 155, no. 6, p. 643–658, doi:10.1007/s00445-008-0250-x.

 Number: 2 Author: Subject: Inserted Text Date: 25/Nov/2015 08:18:58

---

with

84 volcanic rocks, dominated by thick, Plinian pumice fall deposits, with sub-ordinate  
85 intercalated pyroclastic surge and ignimbrite deposits, representing more than 35 km<sup>3</sup> (DRE)  
86 of juvenile material (Tait et al., 2009). <sup>1</sup>A particular characteristic of the Ramadas pumice fall  
87 deposits is the presence of abundant tube pumices (Fig. 2b).

88

89 The pumices are composed of angular lapilli with a texture composed of tubular  
90 bubbles (Marti et al., 1999). The porosity of the undeformed pumice has been estimated at  
91 49-64%, whereas the tube pumice reach 63-78% (Marti et al., 1999). The stretched nature of  
92 tube pumice pores exhibit variable connectivity achieving an anisotropic permeability  
93 ranging from  $\sim 10^{-8}$  m<sup>2</sup> along the stretching axis to  $10^{-13}$  m<sup>2</sup> in the orthogonal direction  
94 (Wright et al., 2006). Up to 40% of the tube pumice exhibit localised kink bands, or box  
95 folds, characterised by couples of parallel dextral and sinistral shear planes, crosscutting the  
96 main pore structure at an angle of 45° (Marti et al., 1999) and thus providing evidence of a  
97 late-stage deformation.

98

99 All pumices present in the deposits show very similar morphological and textural  
100 characteristics - in terms of bubble size, maximum stretching of bubbles, thickness of the  
101 bubble walls - at both, macroscopic and microscopic scales. The sample investigated below  
102 comes from a population of 200 samples that <sup>2</sup>which correspond to the most pristine of all the  
103 samples collected in 5 field seasons between 1985 and 2009. These 200 samples were  
104 selected because they were not partially altered or devitrified due to post-depositional  
105 processes. <sup>3</sup>The sample analysed in this study is highly representative of the eruptive products  
106 in these highly homogeneous deposits of Ramadas volcano. There is no significant textural  
107 variability apart from the existence of the shear deformation in some of them, already  
108 described. The remarkable constancy of the kinematic features of the Ramadas tube pumices

 Number: 1 Author: Subject: Comment on Text Date: 27/Nov/2015 09:19:37  
Can you be more specific? How abundant?

---

 Number: 2 Author: Subject: Cross-Out Date: 25/Nov/2015 08:19:07

---

 Number: 3 Author: Subject: Comment on Text Date: 27/Nov/2015 09:22:28  
Again, it would be important to know which percentage of the deposit is similar to the tube pumice investigated in detail this contribution.

109 is in fact what makes this choice of pumice so especially appropriate for the analysis and  
110 conclusions presented in the present study.

111

### 112 **3 Chemical properties of tube pumice**

113 Extensive petrologic characterisation of the eruptive products provides us with  
114 parameters to constrain their rheological behaviour (e.g., Gauthier et al., 1994). The Ramadas  
115 fallout pumices are peraluminous rhyolite (Table 1). They are mostly aphyric, but the minor  
116 presence of freshly preserved pyralspite garnets, have been used to constrain starting pre-  
117 eruptive conditions to 250-300 MPa and 860-875 °C (Gauthier et al., 1994). The rheological  
118 analysis described below requires first a detailed understanding of water concentration  
119 present in the melt at the point of fragmentation. This was achieved via a combination of  
120 Fourier transform infrared analysis (FTIR) and stable hydrogen and oxygen isotope analysis.

121

#### 122 **3.1 Water speciation in the Ramadas pumice**

123 The water content present in the tube pumice was quantified via micro-FTIR  
124 spectroscopy using a Varian FTS Stingray 7000 Micro Image Analyzer spectrometer at the  
125 Institute for Research on Earth Evolution (IFREE), Japan Agency for Marine Earth Science  
126 and Technology (JAMSTEC). Spectra were collected over 512 scans at a resolution of 8 cm<sup>-1</sup>  
127 using a heated ceramic (globar) infrared source and a Ge-coated KBr beamsplitter. A UMA  
128 600 microscope was coupled to the spectrometer to permit precise focusing of the beam on  
129 the area of interest. The beam path within the spectrometer bench and microscope was  
130 continuously purged with N<sub>2</sub> gas and the laboratory was kept as dry as possible to minimize  
131 any interference from the atmosphere. The glass shards were placed on a H<sub>2</sub>O-free IR-  
132 invisible KBr disk, for which background analyses had been taken. For spot analyses, a  
133 liquid-nitrogen cooled HgCdTe<sub>2</sub> (MCT) detector was used, and the aperture was 50 μm<sup>2</sup>. This

This page contains no comments

134 set up permitted collection of spectra across the mid-IR region (6000–700 cm<sup>-1</sup>). Some  
135 spectra were also extracted from 350×350-μm spectroscopic images, which were collected  
136 following the same procedure as the conventional spot analyses except for the detector, which  
137 was a Varian Inc. Lancer Focal Plane Array (FPA) camera. The FPA camera consists of a  
138 MCT array detector with 4096 channels (64×64), which collect spectra over the spectral  
139 range 4000– 900 cm<sup>-1</sup>. This setup offers a channel (or spectral) resolution of 5.5 μm. Any of  
140 the 4096 spectra from the image could be extracted for individual treatment. [For a more  
141 detailed discussion of spectroscopic imaging and the set up see Wysoczanski and Tani  
142 (2006)].

143

144 The perfect plane-parallel nature of tube pumices' bubble walls mean that the  
145 fragmented glass shards require minimal sample preparation to meet the requirements to be  
146 able to conduct micro-FTIR spectroscopy. Two samples were selected for image and spot (n  
147 = 25) FTIR analysis. Absorbance at the 1628 cm<sup>-1</sup> and 3567 cm<sup>-1</sup> peaks was used to derive  
148 molecular H<sub>2</sub>O contents (hereafter termed H<sub>2</sub>O<sub>m</sub>) and total H<sub>2</sub>O content (hereafter termed  
149 H<sub>2</sub>O<sub>t</sub>) that includes H<sub>2</sub>O<sub>m</sub> as well as OH- species using the modified Beer-Lambert law:

150

$$151 \quad c_i = \frac{M_i \cdot A}{\rho \cdot t \cdot \varepsilon} \quad (1),$$

152

153 where  $c_i$  is the concentration of the species  $i$  (in wt.%),  $M_i$  is the molecular weight of the  
154 species of  $i$  (g·mol<sup>-1</sup>),  $A$  is the absorbance of the relevant vibration band,  $\rho$  is the sample  
155 density (g·l<sup>-1</sup>),  $t$  is the thickness of the area analysed (cm), and  $\varepsilon$  is the molar absorptivity  
156 (l·mol<sup>-1</sup>·cm<sup>-1</sup>). Absorbance was measured as the height of the peaks above a linear baseline.  
157 Sample density was calculated from the oxide composition of the glass, measured by electron  
158 probe micro-analysis (e.g., Lange, 1997). The thickness of the glass shards were estimated

This page contains no comments

159 optically using a Zeiss micrometer. Molar absorptivity coefficients of  $55 \text{ l}\cdot\text{mol}^{-1}\cdot\text{cm}^{-1}$   
160 (Newman et al., 1986) for the  $1628 \text{ cm}^{-1}$   $\text{H}_2\text{O}_m$  peak and  $90 \text{ l}\cdot\text{mol}^{-1}\cdot\text{cm}^{-1}$  (Hauri et al., 2002)  
161 for the  $3567 \text{ cm}^{-1}$   $\text{H}_2\text{O}_t$  peak were used.

162  
163 Volatile distribution images obtained with the FPA camera reveal the homogeneity of water  
164 speciation (Fig. 3). Thin bands with higher concentration are where a second bubble wall,  
165 orthogonal to the plane of view, intersects the main bubble wall. Computation of the water  
166 speciation indicates the presence of 4.78-5.49 wt.%  $\text{H}_2\text{O}_t$  of which ~85% is molecular (Table  
167 2). When compared to the equilibrium model of water speciation for rhyolite compositions  
168 (Zhang, 1999), the obtained water concentration (Fig. 4) shows disequilibrium which  
169 suggests post-emplacement hydration by meteoric water (e.g., Denton et al., 2009). In order  
170 to confirm this we analysed the oxygen and hydrogen isotope compositions of the samples,  
171 which also provides further information on the origin of the meteoric water.

172

### 173 **3.2 Stable H and O isotope in Ramadas Pumice**

174 Stable isotope measurements on two tube pumice samples, one unaltered and the other  
175 slightly weathered, were performed at University of Lausanne, Switzerland. Hydrogen  
176 isotope compositions were determined using a high-temperature ( $1450 \text{ }^\circ\text{C}$ ) reduction method  
177 with He carrier gas and a TC-EA linked to a Delta Plus XL mass spectrometer from Thermo-  
178 Finnigan on 2 to 5 mg sized samples (Sharp et al. 2001). Each sample was measured three  
179 times. Hydrogen contents were calculated from hydrogen voltage signals, sample weights,  
180 and a calibration curve, and are expressed as weight percent water. They have an accuracy of  
181 about  $\pm 0.08 \text{ wt.}\%$   $\text{H}_2\text{O}$ . Oxygen was extracted from 0.5 to 2 mg of sample by heating with a  
182  $\text{CO}_2$ -laser in a  $\text{F}_2$  atmosphere of 50 mbar (Kasemann et al., 2001; Sharp, 1990). An overnight  
183 prefluorination step was conducted to remove easy exchangeable, surface-bound water. The  
184 extracted  $\text{O}_2$  was collected on a molecular sieve ( $5\text{\AA}$ ) and subsequently expanded into a

This page contains no comments

185 Finnigan MAT 253 dual-inlet isotope ratio mass spectrometer. The results are given in the  
186 standard  $\delta$ -notation expressed relative to Vienna standard mean ocean water (VSMOW) in  
187 permil (‰). The accuracy was better than  $\pm 2\%$  for hydrogen and better than  $\pm 0.2\%$  for  
188 oxygen isotope analyses.

189

190 The fresh tube pumice sample has a  $\delta^{18}\text{O}_{\text{VSMOW}}$  value of  $14.0\%$  and  $\delta\text{D}_{\text{VSMOW}}$  values  
191 are  $-129\pm 2\%$ , while the slightly weathered sample is somewhat isotopically lighter with  
192  $13.1\pm 0.2\%$  for oxygen and  $-135\pm 2\%$  for hydrogen isotope values (Table 3). The water  
193 contents are 4.85 wt.% for the fresh and 5.00 wt.% for the slightly weathered sample. The  
194 oxygen and hydrogen isotope data are not consistent with an undegassed primary magmatic  
195 isotope signature (Goff and McMurtry, 2000; Sheppard et al., 1969). They plot in a  $\delta^{18}\text{O}$ - $\delta\text{D}$   
196 diagram (Fig. 5) close to the hydrated volcanic glass line (HVGL) of Taylor (1968). This line  
197 corresponds to isotope compositions of hydrated acidic glasses in equilibrium with meteoric  
198 waters at low temperatures ( $\sim 20^\circ\text{C}$ ). We note that this does not necessarily imply that  
199 anhydrous glasses were hydrated at ambient temperatures (Cerling et al., 1985; Taylor, 1968).  
200 It is possible that glasses that were hydrated at high temperatures and re-equilibrated with  
201 meteoric waters at low temperatures due to diffusive isotope exchange over time scales of  
202 tens of thousand to about one million years (Gilg and Sheppard, 1999). The isotope  
203 composition of waters on the global meteoric water line in equilibrium the two glass samples  
204 can be calculated using the equilibrium isotope fractionation factors of Taylor (1968) and  
205 Friedman et al. (1993) and are  $-12\%$  for  $\delta^{18}\text{O}$  and  $-90\%$  for  $\delta\text{D}$  (Fig. 5). These values are  
206 higher than the local average meteoric waters at an elevation of about 3800 m above sea level  
207 ( $\sim -15\%$ / $-110\%$ ; Fernández et al., 1991; Hoke et al., 2009; Quade et al., 2007; Sharp et al.,  
208 2003). This difference indicates the glasses were isotopically equilibrated at lower elevations  
209 than they are at today, consistent with the uplift history of the Altiplano (Garzzone et al.,

This page contains no comments

210 2008).

211

### 212 **3.3 Magmatic water content at fragmentation**

213 Concluding that most of the water measured in the pumice is derived from post-  
214 eruption hydration by meteoric waters, we turn to the water speciation equilibrium law for  
215 rhyolite compositions (i.e., Zhang, 1999) in order to estimate the original magmatic water  
216 content. Post-eruption hydration is believed to add molecular water without altering the  
217 concentration of the OH-group locked in the structure of a glass (Denton et al., 2009). Thus  
218 we can use the concentration of OH<sup>-</sup> species to extrapolate the total magmatic molecular  
219 water assuming equilibrium speciation (Fig. 6). Here, The OH<sup>-</sup> species concentration of 0.69-  
220 0.78 wt.% is used in the water speciation equilibrium law of Zhang (1999) to constrain a total  
221 magmatic water content of approximately 0.86-1.01 wt.%, which could indicate a pressure as  
222 low as 10 MPa. **Given the likely possibility of isotopic exchange with a higher initially**  
223 **magmatic water content, together with the extreme degassing conditions extant during the**  
224 **formation of tube pumice, we infer significantly higher water contents than this minimum**  
225 **estimate during the shearing flow described here.** Together with the geochemical composition  
226 provided by Gauthier (1994), the water concentration can be used as first order constraint for  
227 the calculation of the rheological properties of the tube pumice necessary at the point of  
228 fragmentation to constrain the underlying shearing regime.

229

### 230 **4 Porous network analysis**

231 Advance in non-destructive tomographic imaging has provided us with a key tool to  
232 detail the internal porous structure of volcanic rocks (Ashwell et al., 2015; Bai et al., 2011;  
233 Baker et al., 2012; Degruyter et al., 2010; Lavallée et al., 2013; Okumura et al., 2008; Wright  
234 et al., 2006). Here, the internal structure of the tube pumice was imaged in 3-D using neutron

 Number: 1 Author: Subject: Comment on Text Date: 27/Nov/2015 09:35:34

The authors should be more specific here. I do not understand how the concentration of H<sub>2</sub>O could be significantly higher than this. Even if the magma is vigorously degassing, how much degassing can occur once magma has been fragmented? If the author cannot estimate how much water was lost from the moment of fragmentation, I would modify the text to say that this values is possibly a lower estimate.

235 computed tomography the ANTARES beamline (FRM-II) in Garching, Germany (Hess et al.,  
236 2011). 800 single radiographs were taken by rotating the sample each time by  $0.45^\circ$  with an  
237 exposure time of 50 seconds at a collimation of 800 (ratio of beam flight length to pinhole  
238 diameter). The neutron beam interaction with the sample was detected by a  $100\ \mu\text{m}$  thick  
239 neutron sensitive scintillation screen (ZnS + LiF). The resulting set of radiographs was then  
240 reconstructed using the inverse radon transformation (Deans, 2007) to generate a 3D image of  
241 the local attenuation within the object with a voxel size  $51.2^3\ \mu\text{m}^3$  (Fig. 7).

242

243 The resulting dataset ( $>12,000$  bubbles) was then segmented using a watershed  
244 algorithm acting on the attenuation gradient in order to accurately map the pores' size, shape  
245 and orientation (Fig. 7; see supplementary material). Except where the bubble coalesced  
246 (which were discarded for the analysis below), bubble walls are generally observed to form a  
247 perfectly closed shell around each pore (Fig. 7c-e). The pores were characterised in terms of  
248 their volumes, aspect ratio ( $l/a$ ), ellipticity ( $1-c/b$ ), orientation ( $\theta$ ) and undeformed radius ( $a$ )  
249 (Fig. 8). Each pore was characterised using a least-squares ellipsoid fit. This fitting was  
250 performed in an automatic fashion using the labelled regions and edges determined by the  
251 segmentation algorithm. The quality of the fitting was manually evaluated by overlaying the  
252 fitted ellipsoid and edge voxels. Poor ellipsoid fits, often due to bubble coalescence, were  
253 excluded.

254

255 The observed geometry of the pore space was numerically modelled to constrain the  
256 conditions of strain rate in the conduits. The steady shapes and orientations of bubbles in a  
257 viscous Newtonian fluid deforming via simple or pure shear can be expressed as a function of  
258 the capillary number ( $Ca$ ):

259

This page contains no comments

260  $Ca = \frac{aG\mu_s}{\Gamma}$  (2),

261

262 where  $a$  is the undeformed bubble radius, and  $G$ ,  $\mu_s$  and  $\Gamma$  are the shear rate, the shear  
263 viscosity and the surface tension of the magma, respectively. The undeformed bubble radius  
264 is calculated from the voxel volume of each pore ( $V$ ) via

265

266  $a = \left(\frac{3}{4\pi}V\right)^{1/3}$  (3).

267

268 Yet, the reconstructed bubbles preserved in the tube pumice may not directly reflect the  
269 bubbles present in the conduit upon fragmentation; that is, after fragmentation, the liquid in  
270 the bubble walls may have some time to relax and the bubble may regain a spherical shape  
271 before the eruptive products freeze in at the glass transition. The effect of relaxation on  
272 bubble radius has been experimentally determined to be:

273

274  $\frac{\ell-a}{\ell_i-a} = \exp\left(\frac{-0.67\Gamma t}{a\mu_s}\right)$  (4),

275

276 where  $\ell$  is the current major radius of the bubble and  $\ell_i$  is the initial major radius (Rust and  
277 Manga, 2002). Although the experimental calibration of these relations have been performed  
278 at lower bulk vesicularity than is exhibited here, and potentially further aspects of bubble-  
279 bubble interactions may ensue at high vesicularities, **we see in these samples no evidence of**  
**280 the latter.** Furthermore, the precedent of applying this treatment at similar levels of  
281 vesicularities is well-established in the recent literature (Moitra et al., 2013). We note that an  
282 experimental calibration at higher vesicularities, using controlled deformation experiments is  
283 clearly a priority for the future. The surface tension at 1 kbar pressure (Bagdassarov et al.,

---

 Number: 1 Author: Subject: Comment on Text Date: 27/Nov/2015 09:40:24  
Can the author specify what would be the evidences of this interaction process?

284 2000) and the viscosity (Hess and Dingwell, 1996) of peraluminous silicate liquid can be  
285 expressed as functions of temperature ( $T$ ) and measured total magmatic water content ( $w$ ):

286

$$287 \quad \Gamma = \frac{-11323.7}{T} + 179.17 \quad (5)$$

288

289 and

290

$$291 \quad \log \mu_s = -3.545 + 0.833 \ln w + \frac{9601 - 2368 \ln w}{T - 195.7 - \ln w} \quad (6).$$

292

293 In our post-fragmentation deformation analysis, we assume that the temperature of the liquid  
294 in the tube pumice follows the Newtonian cooling law,

295

$$296 \quad T = (T_i - T_{env})e^{-kt} + T_{env} \quad (7),$$

297

298 where  $T_i$  is the initial temperature (set by geothermometry at 860-875 °C),  $T_{env}$  is the  
299 temperature of the environment (20 °C), and  $k$  is the characteristic cooling rate defined by the  
300 following cooling rate experiment: A thermocouple was embedded in the center of the tube  
301 pumice block used for tomography that was then subjected to cooling from 850°C to room  
302 temperature while recording upon removal from the furnace; using Eq. (7) the characteristic  
303 cooling rate was constrained to  $10^{-4.9} \text{ s}^{-1}$ . The integration of Eq. (2) through (7) provides us  
304 with the capillary number of bubbly magmas, which may be assessed for bubble orientation  
305 and deformation in pure or simple shear flows <sup>1</sup>for high and low deformation regimes (Table  
306 4; Rust et al., 2003). We ultimately obtain expressions for the evolution of bubbles' shape  
307 and orientations. Extrapolation of these expressions to an arbitrarily large time allows the  
308 shape and orientation of pores in a tube pumice formed under each shear scenario to be



309 predicted. Note that by fixing the characteristic cooling rate, the water content remains the  
310 only free fit parameter. The results of that fitting yield water contents consistent with the  
311 discussion above.

312

313 The 3D dataset reveals that bubble orientation with respect to the flow direction as  
314 well as the major axis length varies with the undeformed bubble radius (Fig. 9). From the  
315 mechanical scenarios that we have envisaged, the bubbles in a pure shear regime would  
316 implicitly stretch with the flow direction regardless of their initial size, whereas in a simple  
317 shear regime they would stretch according to the local stress, which will not necessarily be  
318 parallel to the flow direction. It is thus abundantly evident (Fig. 9a) that the bubble  
319 orientation matches the expected distribution from a simple shear mechanism, best  
320 constrained by a strain rate of  $10^{-2} \text{ s}^{-1}$ . Numerically, it was only possible to fit the observed  
321 bubble elongation using a simple shear model, whereas pure shear required non-physical  
322 values of strain rates and an infinitely fast cooling rate in order to fit some of the  
323 observations. In the simple shear model, we observe that internal heat transport can account  
324 for the entire data distribution (Fig 9b). Thus the model indicates that simple shear controls  
325 the late fate of the porous network of the tube pumice immediately preceding explosive  
326 fragmentation.

327

### 328 **5 Simple shear in volcanic conduits**

329 The dominance of simple shear in the generation of tube pumice of the Ramadas  
330 Plinian phase, speaks of its significance in the magma column. Geometrically, we may view  
331 tube pumice as an estimate of the simple shear in the conduit flow. In a mechanistic sense,  
332 this simple shear strain, drives the extremely fast ascent rates prior to fragmentation (Castro  
333 and Dingwell, 2009). Indeed, the formation of tube pumice in marginal areas of strain

---

 Number: 1 Author: Subject: Comment on Text Date: 27/Nov/2015 09:48:24

This part is not clear to me. See General comments.

334 localisation suggests that the principal stress was sub-parallel to flow direction and not  
335 parallel, as proposed in our previous study (Marti et al., 1999).

336

337         The preservation of kink bands forming angular box folds in the pumice further  
338 highlights the need for fluctuations in compressional deformation axial to the stretching  
339 direction of the bubbles. Whereas the stretched bubbles record the pervasive, or ductile,  
340 nature of deformation in the marginal areas of a plug flow, the kink bands, with their  
341 localised character akin to a box fold, entail a stronger and presumably shorter compressional  
342 event in the direction of a highly anisotropic medium. Here we speculate that their triggering  
343 mechanism is the very late stage passage of shock fronts generated during the explosions  
344 accompanying fragmentation, as an earlier generation of kink bands would have been  
345 subjected to further deformation and offsetting, although other unexplored mechanisms of  
346 very late stage generation might be feasible.

347

348         If tube pumices are indeed a strain marker of the ductile-brittle transition of magma  
349 upon fragmentation, they may thus provide us with the information required to reconstruct  
350 the shearing mode distribution that drives explosive eruptions. Increased simple shearing of  
351 the bubble network may eventually accentuate the permeability and vertical degassing of the  
352 magma in the conduit (Wright et al., 2006; Wright and Weinberg, 2009). The effects of such  
353 shearing in the conduit may favour a shift of the fragmentation level in the magma column to  
354 greater depths and higher pressures as has evidently been the case at Ramadas. Upon  
355 fragmentation, compressive shocks released in the marginal magmas may generate kinks,  
356 which offset the tubular bubbles and upset the degassing network, subsequently leading to  
357 fragmentation and generation of tube pumices. We conclude that an overlying and overriding  
358 simple shear strain in magma (accompanied in this case by kink band generation) is a major

This page contains no comments

359 regulator of ascent dynamics and fragmentation front stabilisation. Major kinematic  
360 campaigns of eruptive products will be necessary in order to perform the global comparison  
361 of eruptive dynamics unlocked by these techniques.

362  
363

364 **Supplementary material related to this article is available online at**

365

366 *Author Contributions.* D.B.D., K-U.H., Y.L. designed the experiments. K-U.H. and B.S.  
367 performed the tomographic scans and A.F. analysed and modelled them. A.R.L.N. and Y.L.  
368 analysed the water content and H.A.G. the isotopes composition. J.M. performed fieldwork  
369 and collected samples. All authors contributed to the study.

370

371

372 *Acknowledgements.* We thank Thomas Shea for constructively reviewing an earlier version of  
373 this manuscript. Financial support was provided by the Deutsche Forschungsgemeinschaft  
374 (DFG) – International Continental Drilling Program (ICDP) grant HE 4565-2-1 as well as the  
375 DFG grants LA 2651-1-1 and LA 2651 3-1. Y.L. acknowledges support from the European  
376 Research Council (ERC) for the Starting Grant on *Strain Localisation in Magmas* (SLiM,  
377 nbr. 306488). D.B.D. acknowledges a Research Professorship in Experimental Volcanology  
378 of the Bundesezellenzinitiative (LMUexcellent) as well as an ERC Advanced Grant on  
379 *Explosive Volcanism in the Earth System* (EVOKES, nbr. 247076).

380

381

## 382 **References**

- 383 Ashwell, P. A., Kendrick, J. E., Lavallée, Y., Kennedy, B. M., Hess, K. U., von Aulock, F.  
384 W., Wadsworth, F. B., Vasseur, J., and Dingwell, D. B.: Permeability of compacting porous  
385 lavas, *Journal of GEophysical Research-Solid Earth*, 2015. 2015.  
386 Bagdassarov, N., Dorfman, A., and Dingwell, D. B.: Effect of alkalis, phosphorus, and water  
387 on the surface tension of haplogranite melt, *American Mineralogist*, 85, 33-40, 2000.  
388 Bai, L. P., Baker, D. R., and Hill, R. J.: Permeability of vesicular Stromboli basaltic glass:  
389 Lattice Boltzmann simulations and laboratory measurements, *Journal of Geophysical*

This page contains no comments

390 Research-Solid Earth, 115, 2011.

391 Baker, D. R., Brun, F., O'Shaughnessy, C., Mancini, L., Fife, J. L., and Rivers, M.: A four-  
392 dimensional X-ray tomographic microscopy study of bubble growth in basaltic foam,  
393 Nature Communications, 3, 2012.

394 Caricchi, L., Pommier, A., Pistone, M., Castro, J., Burgisser, A., and Perugini, D.: Strain-  
395 induced magma degassing: insights from simple-shear experiments on bubble bearing  
396 melts, Bulletin of Volcanology, 73, 1245-1257, 2011.

397 Casas, A., Hernandez, E., Marti, J., and Petrinovic, I.: Gravity modelling of the Ramadas  
398 Caldera (Argentinean Puna, Central Andes), 4<sup>o</sup> Congreso Internacional Da Sociedade  
399 Brasileira de Geofisica, 1995. 1995.

400 Castro, J. M. and Dingwell, D. B.: Rapid ascent of rhyolitic magma at Chaiten volcano,  
401 Chile, Nature, 461, 780-784, 2009.

402 Cerling, T. E., Brown, F. H., and R., B. J.: Low-temperature alteration of volcanic glass:  
403 hydration, Na, K, <sup>18</sup>O and Ar mobility Chemical Geology (Isotope Geoscience Section), 52,  
404 281-293, 1985.

405 Collinson, A. S. D. and Neuberg, J. W.: Gas storage, transport and pressure changes in an  
406 evolving permeable volcanic edifice, Journal of Volcanology and Geothermal Research,  
407 243, 1-13, 2012.

408 Compton, J. S., Conrad, M. E., and Vennemann, T. W.: Stable isotope evolution of volcanic  
409 ash layers during diagenesis of the Miocene Monterey formation, California, Clays and  
410 Clay Minerals, 47, 84-95, 1999.

411 Deans, S. R.: The radon transform and some of its applications, Dover Publishing Co, New  
412 York, 2007.

413 Degruyter, W., Bachmann, O., and Burgisser, A.: Controls on magma permeability in the  
414 volcanic conduit during the climactic phase of the Kos Plateau Tuff eruption (Aegean Arc),  
415 Bulletin of Volcanology, 72, 63-74, 2010.

416 Denton, J. S., Tuffen, H., Gilbert, J. S., and Odling, N.: The hydration and alteration of perlite  
417 and rhyolite from Iceland, Journal of the Geological Society of London, 166, 895-904,  
418 2009.

419 Fernández, J., Markgraf, V., Panarello, H. E., Albero, M., Angiolini, F. E., Valencio, S., and  
420 Arriaga, M.: Late Pleistocene/Early Holocene environments and climates, fauna, and human  
421 occupation in the Argentine Altiplano, Geoarchaeology, 6, 251-272, 1991.

422 Friedman, I., Gleason, J., Sheppard, R. A., and Gude, A. J. r.: Deuterium fractionation as  
423 water diffuses into silicic volcanic ash. In: Climate change and continental isotopic records,  
424 Swart, P. K., Lohmann, K. C., McKenzie, J., and Savin, S. (Eds.), Geophysical Monograph,  
425 American Geophysical Union, 1993.

426 Garzione, C. N., Hoke, G. D., Libarkin, J. C., Withers, S., MacFadden, B., Eiler, J., Gosh, P.,  
427 and Mulch, A.: Rise of the Andes, Science, 320, 1304-1307, 2008.

428 Gauthier, P. J., Deruelle, B., Viramonte, J., and Aparicio, A.: Garnets from La Pava-Ramadas  
429 rhyolite (NW Argentina) and from its granite xenoliths, Comptes Rendus De L Academie  
430 Des Sciences Serie Ii, 318, 1629-1635, 1994.

431 Gilg, H. A. and Sheppard, S. M. F.: Stability of H and O isotope ratios in natural hydrated  
432 silicic glasses: estimation of diffusion coefficient for water at ambient temperatures, Journal  
433 of Conference Abstracts, Proceedings of EUG 10, Strasbourg, France, March 28th – April  
434 1st, 4, 531, 1999.

435 Goff, F. and McMurtry, G. M.: Tritium and stable isotopes of magmatic waters, Journal of  
436 Volcanology and Geothermal Research, 97, 347-396, 2000.

437 Hauri, E., Wang, J. H., Dixon, J. E., King, P. L., Mandeville, C., and Newman, S.: SIMS  
438 analysis of volatiles in silicate glasses 1. Calibration, matrix effects and comparisons with  
439 FTIR, Chemical Geology, 183, 99-114, 2002.

This page contains no comments

440 Hess, K. U. and Dingwell, D. B.: Viscosities of hydrous leucogranitic melts: A non-  
441 Arrhenian model, *American Mineralogist*, 81, 1297-1300, 1996.

442 Hess, K. U., Flaws, A., Muehlbauer, M. J., Schillinger, B., Franz, A., Schulz, M., Calzada, E.,  
443 Dingwell, D. B., and Bente, K.: Advances in high-resolution neutron computed  
444 tomography: Adapted to the earth sciences, *Geosphere*, 7, 1294-1302, 2011.

445 Hoke, G. D., Garzione, C. N., Araneo, D. C., Latorre, C., Strecker, M. R., and Williams, K.  
446 J.: Stable isotope altimeter: Do Quaternary pedogenic carbonates predict modern  
447 elevations?, *Geology*, 37, 1015-1018, 2009.

448 Kasemann, S., Meixner, A., Rocholl, A., Vennemann, T., Schmitt, A., and Wiedenbeck, M.:  
449 Boron and oxygen isotope composition of certified reference materials NIST SRM 610/612,  
450 and reference materials JB-2G and JR-2G, *Geostandards Newsletter*, 25, 405-416, 2001.

451 Kendrick, J. E., Lavallée, Y., Hess, K. U., Heap, M. J., Gaunt, H. E., Meredith, P. G., and  
452 Dingwell, D. B.: Tracking the permeable porous network during strain-dependent magmatic  
453 flow, *Journal of Volcanology and Geothermal Research*, 260, 117-126, 2013.

454 Klug, C. and Cashman, K. V.: Permeability development in vesiculating magmas:  
455 Implications for fragmentation, *Bulletin of Volcanology*, 58, 87-100, 1996.

456 Koyaguchi, T., Scheu, B., Mitani, N. K., and Melnik, O.: A fragmentation criterion for highly  
457 viscous bubbly magmas estimated from shock tube experiments, *Journal of Volcanology  
458 and Geothermal Research*, 178, 58-71, 2008.

459 Lange, R. A.: A revised model for the density and thermal expansivity of K<sub>2</sub>O-Na<sub>2</sub>O-CaO-  
460 MgO-Al<sub>2</sub>O<sub>3</sub>-SiO<sub>2</sub> liquids from 700 to 1900 K: extension to crustal magmatic temperatures,  
461 *Contributions to Mineralogy and Petrology*, 130, 1-11, 1997.

462 Lavallée, Y., Benson, P. M., Heap, M. J., Hess, K.-U., Flaws, A., Schillinger, B., Meredith, P.  
463 G., and Dingwell, D. B.: Reconstructing magma failure and the degassing network of dome-  
464 building eruptions, *Geology*, 41, 515-518, 2013.

465 Mader, H. M., Phillips, J. C., Sparks, R. S. J., and Sturtevant, B.: Dynamics of explosive  
466 degassing of magma: Observations of fragmenting two-phase flows, *Journal of Geophysical  
467 Research-Solid Earth*, 101, 5547-5560, 1996.

468 Marti, J., Soriano, C., and Dingwell, D. B.: Tube pumices as strain markers of the ductile-  
469 brittle transition during magma fragmentation, *Nature*, 402, 650-653, 1999.

470 Moitra, P., Gonnermann, H. M., Houghton, B. F., and Giachetti, T.: Relating vesicle shapes  
471 in pyroclasts to eruption styles, *Bulletin of Volcanology*, 75, 691-691, 2013.

472 Neuberg, J. W., Tuffen, H., Collier, L., Green, D., Powell, T., and Dingwell, D.: The trigger  
473 mechanism of low-frequency earthquakes on Montserrat, *Journal of Volcanology and  
474 Geothermal Research*, 153, 37-50, 2006.

475 Newman, S., Stolper, E. M., and Epstein, S.: Measurement of water in rhyolitic glasses -  
476 Calibration of an infrared spectroscopic technique, *American Mineralogist*, 71, 1527-1541,  
477 1986.

478 Okumura, S., Nakamura, M., Tsuchiyama, A., Nakano, T., and Uesugi, K.: Evolution of  
479 bubble microstructure in sheared rhyolite: Formation of a channel-like bubble network,  
480 *Journal of Geophysical Research-Solid Earth*, 113, 2008.

481 Papale, P.: Strain-induced magma fragmentation in explosive eruptions, *Nature*, 397, 425-  
482 428, 1999.

483 Pistone, M., Caricchi, L., Ulmer, P., Burlini, L., Ardia, P., Reusser, E., Marone, F., and  
484 Arbaret, L.: Deformation experiments of bubble- and crystal-bearing magmas: Rheological  
485 and microstructural analysis, *Journal of Geophysical Research-Solid Earth*, 117, 2012.

486 Polacci, M.: Constraining the dynamics of volcanic eruptions by characterization of pumice  
487 textures, *Annals of Geophysics*, 48, 731-738, 2005.

488 Proussevitch, A. A. and Sahagian, D. L.: Dynamics and energetics of bubble growth in  
489 magmas: Analytical formulation and numerical modeling, *Journal of Geophysical Research-*

This page contains no comments

490 Solid Earth, 103, 18223-18251, 1998.

491 Proussevitch, A. A., Sahagian, D. L., and Kutolin, V. A.: Stability of foams in silicate melts,  
 492 Journal of Volcanology and Geothermal Research, 59, 161-178, 1993.

493 Quade, J., Garzione, C., and Eiler, J.: Paleoelevation reconstruction using pedogenic  
 494 carbonates, Reviews in Mineralogy and Geochemistry, 66, 53-87, 2007.

495 Rust, A. C. and Cashman, K. V.: Permeability controls on expansion and size distributions of  
 496 pyroclasts, Journal of Geophysical Research-Solid Earth, 116, 17, 2011.

497 Rust, A. C. and Cashman, K. V.: Permeability of vesicular silicic magma: inertial and  
 498 hysteresis effects, Earth and Planetary Science Letters, 228, 93-107, 2004.

499 Rust, A. C. and Manga, M.: Bubble shapes and Orientations in low Re simple shear flow,  
 500 Journal of Colloid and Interface Science, 249, 476-480, 2002.

501 Rust, A. C., Manga, M., and Cashman, K. V.: Determining flow type, shear rate and shear  
 502 stress in magmas from bubble shapes and orientations, Journal of Volcanology and  
 503 Geothermal Research, 122, 111-132, 2003.

504 Sahagian, D.: Volcanology - Magma fragmentation in eruptions, Nature, 402, 589+, 1999.

505 Sharp, Z. D.: A laser-based microanalytical method for the in-situ determination of oxygen  
 506 isotope ratios of silicates and oxides, Geochimica et Cosmochimica Acta, 54, 1353-1357,  
 507 1990.

508 Sharp, Z. D., Atudorei, V., Panarello, H. O., Fernández, J., and Douthitt, C.: Hydrogen  
 509 isotope systematics of hair: archeological and forensic applications, Journal of  
 510 Archaeological Science, 30, 1709-1716, 2003.

511 Sheppard, S. M. F., Nielson, R. L., and Taylor, H. P. J.: Oxygen and hydrogen isotope ratios  
 512 of clay minerals from porphyry copper deposits, Economic Geology, 64, 755-777, 1969.

513 Spieler, O., Dingwell, D. B., and Alidibirov, M.: Magma fragmentation speed: an  
 514 experimental determination, Journal of Volcanology and Geothermal Research, 129, 109-  
 515 123, 2004.

516 Tait, M. A., Cas, R. A. F., and Viramonte, J. G.: The origin of an unusual tuff ring of perlitic  
 517 rhyolite pyroclasts: The last explosive phase of the Ramadas Volcanic Centre, Andean  
 518 Puna, Salta, NW Argentina, Journal of Volcanology and Geothermal Research, 183, 1-16,  
 519 2009.

520 Taylor, B. E., Eichelberger, J. C., and Westrich, H. R.: Hydrogen isotopic evidence for  
 521 rhyolitic magma degassing during shallow intrusion and eruption, Nature, 306, 541-545,  
 522 1983.

523 Taylor, H. P. J.: The oxygen isotope geochemistry of igneous rocks, Contribution to  
 524 Mineralogy and Petrology, 19, 1-71, 1968.

525 Viramonte, J. G., Omarini, R. H., Araña Saavedra, V., Aparicio, A., García Cacho, L., and  
 526 Párica, P.: Edad, génesis y mecanismos de erupción de las riolitas granatíferas de San  
 527 Antonio de los Cobres, Provincia de Salta, IX Congr. Geol. Arg. Actas, 3, 216-233, 1984.

528 Wright, H. M. N., Roberts, J. J., and Cashman, K. V.: Permeability of anisotropic tube  
 529 pumice: Model calculations and measurements, Geophysical Research Letters, 33, 2006.

530 Wright, H. M. N. and Weinberg, R. F.: Strain localization in vesicular magma: Implications  
 531 for rheology and fragmentation, Geology, 37, 1023-1026, 2009.

532 Wyczoński, R. and Tani, K.: Spectroscopic FTIR imaging of water species in silicic  
 533 volcanic glasses and melt inclusions: An example from the Izu-Bonin arc, Journal of  
 534 Volcanology and Geothermal Research, 156, 302-314, 2006.

535 Zhang, Y. X.: H<sub>2</sub>O in rhyolitic glasses and melts: Measurement, speciation, solubility, and  
 536 diffusion, Reviews of Geophysics, 37, 493-516, 1999.

537

538

This page contains no comments

539 Table 1. Normalised, average chemical analysis of Ramadas obsidian rocks from  
540 Gauthier (1994).

<u>Oxides</u>	<u>Weight %</u>
SiO <sub>2</sub>	75.47
Al <sub>2</sub> O <sub>3</sub>	14.02
Na <sub>2</sub> O	3.85
K <sub>2</sub> O	4.78
MgO	0.01
CaO	0.56
TiO <sub>2</sub>	0.01
FeO (T)	1.12
MnO	0.11
P <sub>2</sub> O <sub>5</sub>	0.05
<u>Total</u>	<u>100.00</u>

541  
542

This page contains no comments

543 Table 2. Water content estimated by FTIR.

Sample	image	row	column	WEIGHT PERCENTS			
				OH <sup>-</sup>	mol H <sub>2</sub> O 1630cm <sup>-1</sup>	total H <sub>2</sub> O 3500cm <sup>-1</sup>	Estimated magmatic H <sub>2</sub> O
TPRT-1	A	4	48	0.88	4.34	5.22	1.19
TPRT-1	A	10	46	0.80	4.46	5.26	1.05
TPRT-1	A	18	50	0.68	4.87	5.55	0.85
TPRT-1	A	30	53	0.63	5.01	5.64	0.76
TPRT-1	A	39	55	0.65	4.74	5.39	0.80
TPRT-1	B	58	44	0.69	4.78	5.46	0.86
TPRT-1	B	2	33	0.72	4.74	5.46	0.92
TPRT-1	B	9	34	0.78	4.66	5.44	1.03
TPRT-1	B	47	41	0.79	4.90	5.69	1.04
TPRT-1	B	16	35	0.65	4.95	5.59	0.79
TPRT-1	C	22	25	0.82	4.81	5.64	1.09
TPRT-1	C	41	30	0.79	4.84	5.63	1.04
TPRT-1	C	55	35	0.72	4.78	5.49	0.91
TPRT-1	C	10	24	0.69	4.79	5.48	0.86
TPRT-1	C	26	30	0.59	4.93	5.52	0.69
TPRT-1	D	9	35	0.54	4.87	5.41	0.60
TPRT-1	D	18	43	0.72	4.84	5.55	0.91
TPRT-1	D	53	52	0.67	4.87	5.55	0.83
TPRT-1	D	30	43	0.66	4.89	5.55	0.81
TPRT-1	D	2	36	0.89	4.83	5.71	1.20
TPRT-1	E	11	32	0.66	4.89	5.55	0.81
TPRT-1	E	23	36	0.65	4.90	5.55	0.79
TPRT-1	E	37	33	0.23	4.97	5.21	0.08
TPRT-1	E	47	36	0.52	4.89	5.40	0.56
TPRT-1	E	59	38	0.78	4.62	5.39	1.01
<b>AVERAGE</b>				<b>0.69</b>	<b>4.81</b>	<b>5.49</b>	<b>0.86</b>
TPRT-2	A	28	20	0.92	3.72	4.64	1.26
TPRT-2	A	30	22	0.85	3.76	4.60	1.13
TPRT-2	A	23	32	0.92	3.59	4.51	1.26
TPRT-2	A	21	33	0.73	3.97	4.70	0.92
TPRT-2	A	21	21	0.79	4.08	4.87	1.03
TPRT-2	B	38	16	0.79	3.79	4.58	1.04
TPRT-2	B	34	11	0.78	4.07	4.85	1.02
TPRT-2	B	15	45	0.81	3.97	4.78	1.06
TPRT-2	B	8	52	0.96	3.90	4.86	1.32
TPRT-2	B	22	31	0.64	4.15	4.79	0.77
TPRT-2	B	18	38	0.67	3.46	4.13	0.83
TPRT-2	C	30	16	0.73	3.35	4.08	0.94
TPRT-2	C	26	24	0.81	4.10	4.91	1.07
TPRT-2	C	23	37	0.58	4.05	4.63	0.68
TPRT-2	C	16	51	0.63	3.94	4.56	0.75
TPRT-2	C	10	58	0.85	4.36	5.22	1.15
TPRT-2	D	31	10	0.80	4.02	4.82	1.05
TPRT-2	D	20	37	0.68	4.23	4.91	0.84

This page contains no comments

TPRT-2	D	12	52	0.81	4.13	4.94	1.06
TPRT-2	D	26	23	0.86	4.02	4.88	1.16
TPRT-2	D	19	41	0.69	4.20	4.89	0.86
TPRT-2	E	12	50	0.74	4.25	4.99	0.96
TPRT-2	E	15	45	0.78	4.18	4.96	1.02
TPRT-2	E	20	35	0.77	4.30	5.06	0.99
TPRT-2	E	17	44	0.68	4.28	4.96	0.85
TPRT-2	E	24	33	0.91	4.23	5.15	1.25
<b>AVERAGE</b>				<b>0.78</b>	<b>4.00</b>	<b>4.78</b>	<b>1.01</b>

544  
545

This page contains no comments

546 Table 3. H and O isotope information.

Sample	$\delta^{18}\text{O}_{\text{VSMOW}}$ (‰)	$\delta\text{D}_{\text{VSMOW}}$ (‰)	H (wt. % $\text{H}_2\text{O}$ )
JM RAM L (fresh)	14.0	-127	4.81
		-131	4.83
		-131	4.91
JM RAM W (weathered)	12.9 13.3	-135	5.06
		-133	5.07
		-136	4.89

547

548

This page contains no comments

549 Table 4. Bubble deformation and orientation for pure shear and simple shear scenarios as  
 550 compiled by Rust et al. (2003) and reference therein.  $a, c, l$  are the semi-principal axes of the  
 551 deformed bubbles (see Fig. 8a).  $D = (l-b)/(l+b)$ . \* The constant of proportionality in the  
 552 bubble deformation equation for  $l/a \gg 1$  assumes that  $P/G\mu_s=2$ , where  $P$  is the pressure in  
 553 the bubble.

Geometrical conditions	Pure shear	Simple shear
Bubble deformation: $Ca \ll 1$	$D = 2Ca$	$D = Ca$
Bubble deformation: $l/a \gg 1$	$l/a = 16Ca^2$ *	$lla = 3.45Ca^{1/2}$
Bubble orientation: $Ca \ll 1$	$\theta = 0$	
Bubble orientation: $l/a \gg 1$	$\theta = 0$	$\theta = \tan^{-1}(0.359Ca^{-3/4})$

554

This page contains no comments

555 **Figure caption**

556

557 Fig. 1. Eruptive shearing. a) Schematic view of magma shearing during eruptions. Strain  
558 localisation along the conduit margins promotes a heterogeneous velocity gradient, which  
559 induces simple shearing (blue) and stretching of bubbles (white ellipses). In the core of the  
560 magma column, a relatively low velocity gradient leaves the bubbles mostly undisturbed and  
561 near isotropic. Relatively rapid decompression increases bubble pressure, which, if exceeding  
562 the magmastatic pressure, will force the bubbles into a tensional regime, which may promote  
563 pure shear. The deformed bubble shape can be characterised by the semi-principle axes of a  
564 best-fit ellipsoid  $l$ ,  $b$ , and  $c$  (modified from Rust et al., 2003).

565

566 Fig. 2. a) Location of the Ramadas Volcanic Complex (RVC) in the Altiplano-Puna Plateau,  
567 Argentina. b) Photograph of a tube pumice from the Ramadas fallout deposit. Coin as scale:  
568 20 mm diameter.

569

570 Fig. 3. Water distribution in two bubble wall fragments: a-b) TPRT1 and c-d) TPRT2.  
571 a) and c) show absorbance of the  $3567\text{ cm}^{-1}$  band, and b) and d) absorbance of the  $1628$   
572  $\text{cm}^{-1}$  band. The composite reconstruction is made of FTIR images of  $350 \times 350\ \mu\text{m}$  (for  
573 each box).

574

575

576 Fig. 4. Speciation of water for bubble wall samples a) TPRT1 and b) TPRT2, plotted  
577 against the equilibrium speciation model for rhyolites of Zhang (1999).

578

579 Fig. 5. Oxygen and hydrogen isotope composition of tube pumice (stars; L : fresh glass,  
580 W : weathered sample), meteoric waters in equilibrium with the glasses, and present-

This page contains no comments

581 day local meteoric waters. Primary Magmatic Waters from Sheppard et al<sup>42</sup>, Degassing  
582 trend (green arrow) from Taylor et al. (1983), HVGL: hydrated volcanic glass line from  
583 Taylor (1968), grey circles: hydrated silicic volcanic glasses from Taylor (1968),  
584 Cerling et al. (1985) and Compton et al. (1999); SMOW: Standard Mean Ocean Water;  
585 GMWL: Global Meteoric Water Line.

586

587 Fig. 6. Total magmatic water extrapolated from the OH<sup>-</sup> concentrations measured by  
588 FTIR using the equilibrium speciation model for rhyolites of Zhang (1999).

589

590 Fig. 7. NCT reconstruction of the tube pumice showing the internal structure of the tubular  
591 texture a) in parallel and b) perpendicular cross sections. c) Rendering of a sub-volume taken  
592 from the tube pumice NCT. d) Cut away of the rendering shown in (c), revealing some of the  
593 internal structure of the sub-volume e) A false-colour composite showing the result of the  
594 segmentation algorithm. Here each pore has been colour coded based on its volume, with  
595 small pores shaded blue increasing through the colour spectrum to large pores, which are  
596 shaded red; voxel size is 51.2\*51.2\*51.2  $\mu\text{m}^3$  (i.e., about 7 mm<sup>3</sup>).

597

598 Fig. 8. Parametrisation of pores. a) Geometry used to parameterise the pores.  
599 Distribution of the frequency of pores identified with b) different orientation and c)  
600 ellipticity.

601

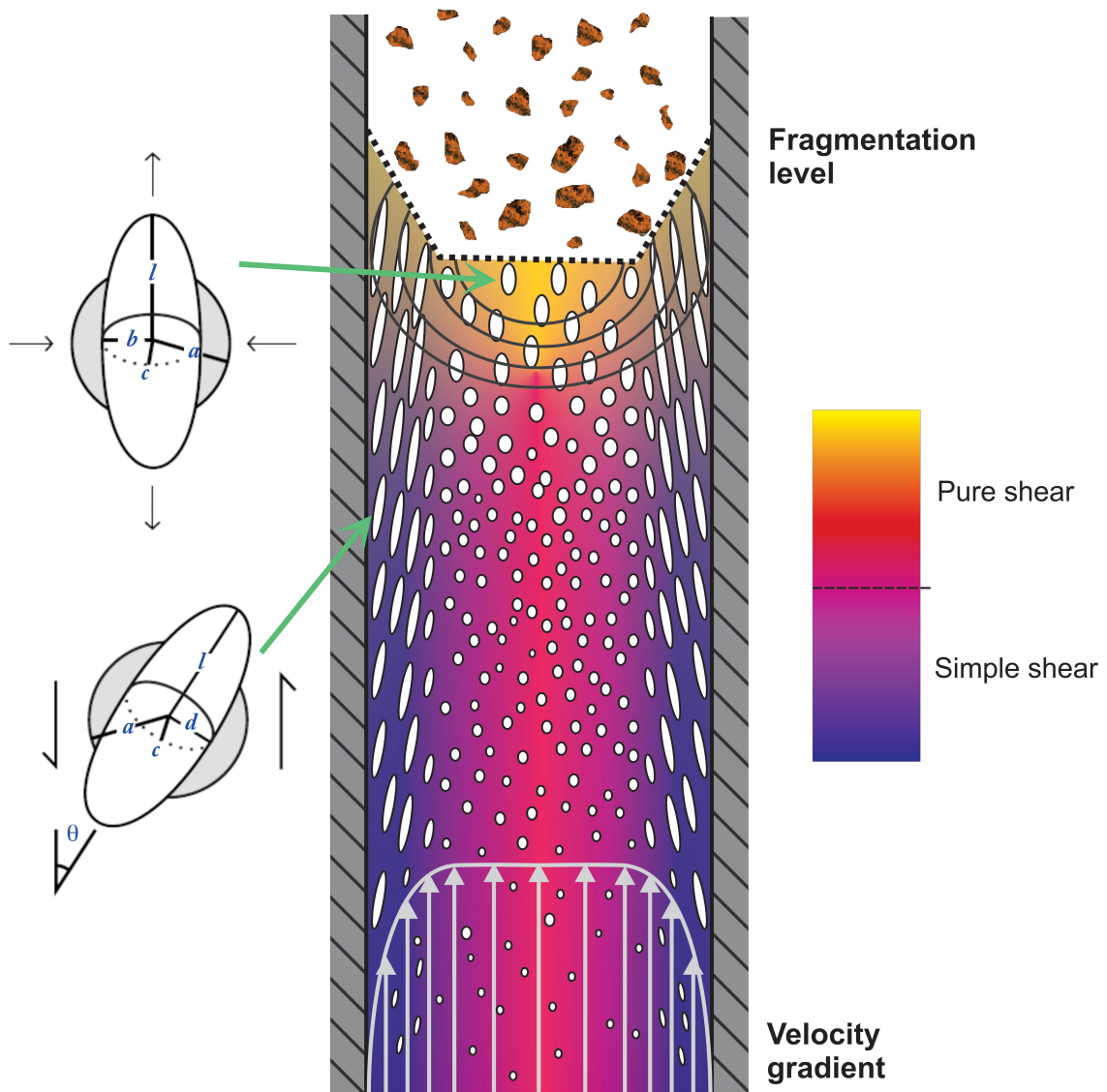
602 Fig. 9. Bubble geometry population and shear models. Bubble geometry distribution  
603 compared to a) the best fit for simple (red) and pure shear (green). b) The best fit for simple  
604 shear requires a characteristic cooling rate of  $10^{-4.9} \text{ s}^{-1}$  and a strain rate of  $10^{-2} \text{ s}^{-1}$ . Applying a  
605 cooling rate profile across the sample explains the data distribution. The best fit for pure

This page contains no comments

606 shear requires a non-physical, infinitely fast, cooling rate; a realistic cooling rate pushes the  
607 modelled bubble length to below the imaged population, rejecting the possibility that pure  
608 shear induced the porous structure of the tube pumice.

This page contains no comments

609 Figure 1

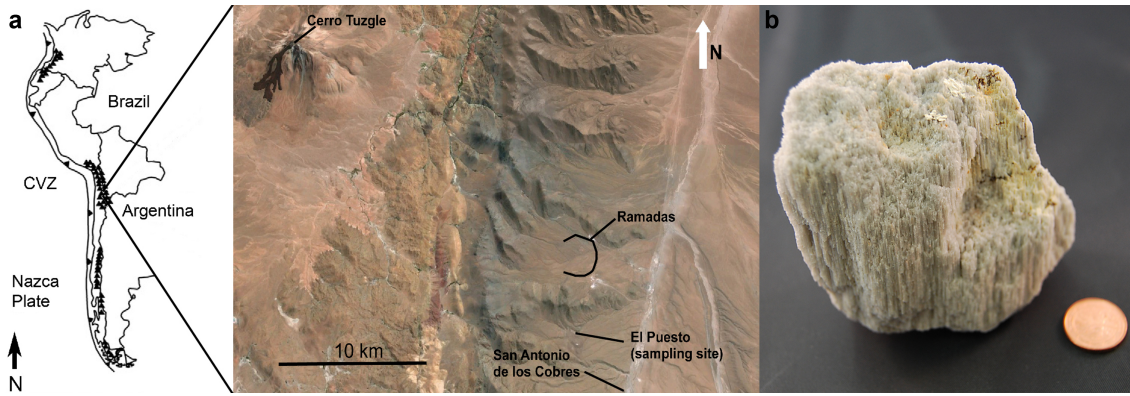


610

611

This page contains no comments

612 Figure 2

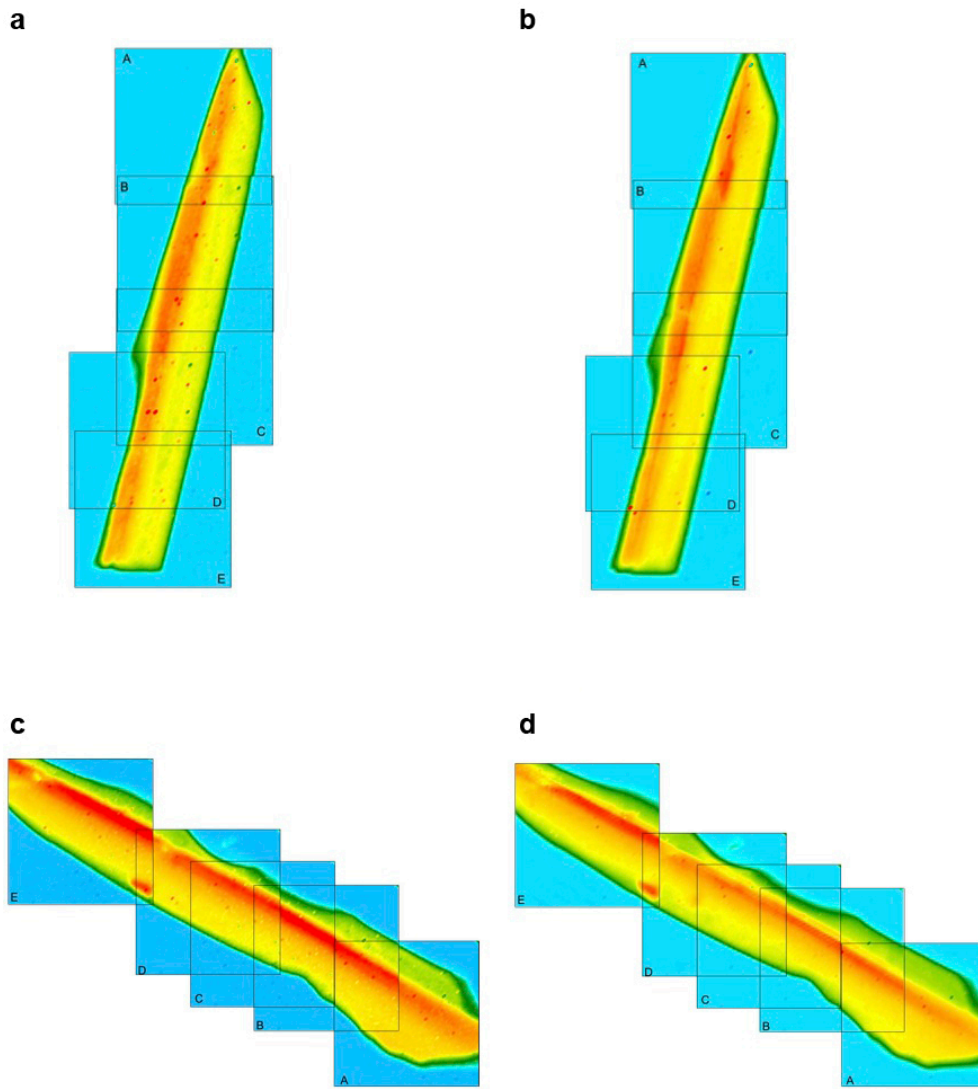


613

614

This page contains no comments

615 Figure 3

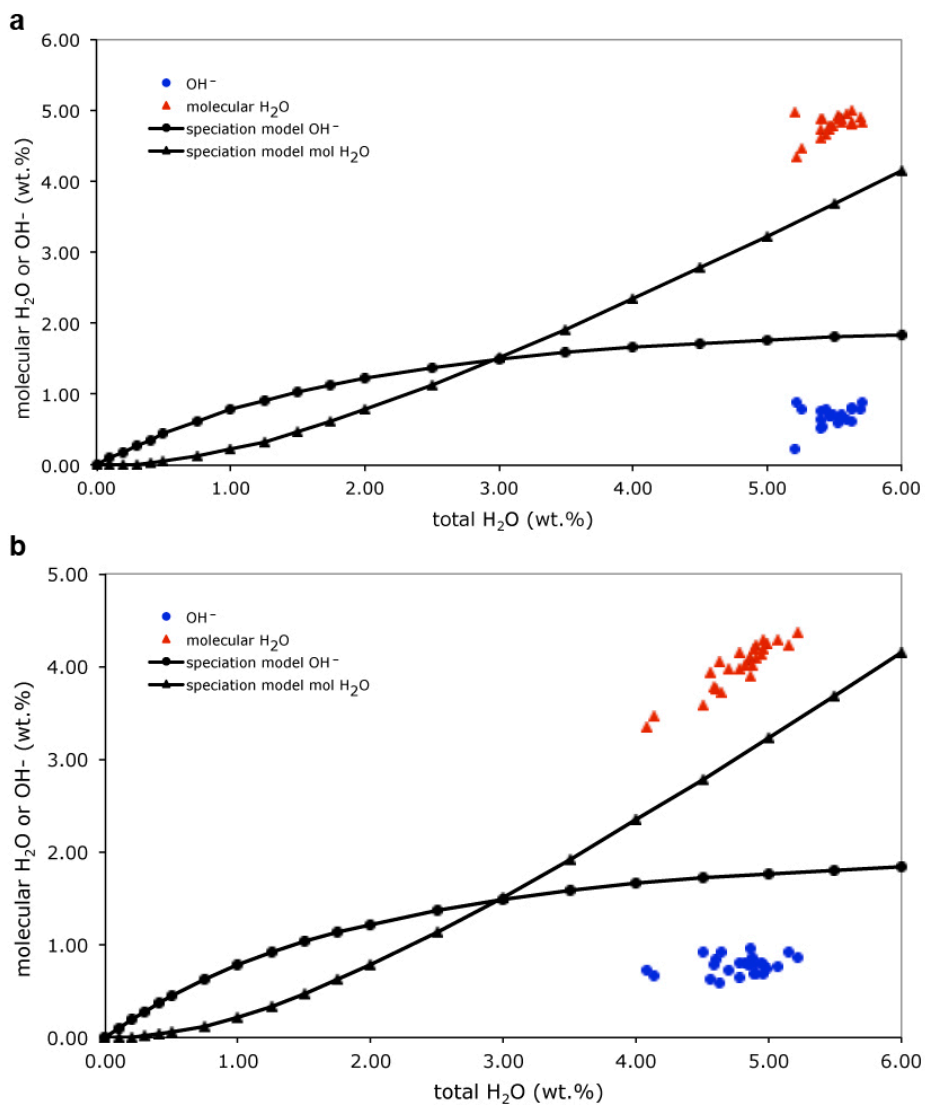


616

617

This page contains no comments

618 Figure 4

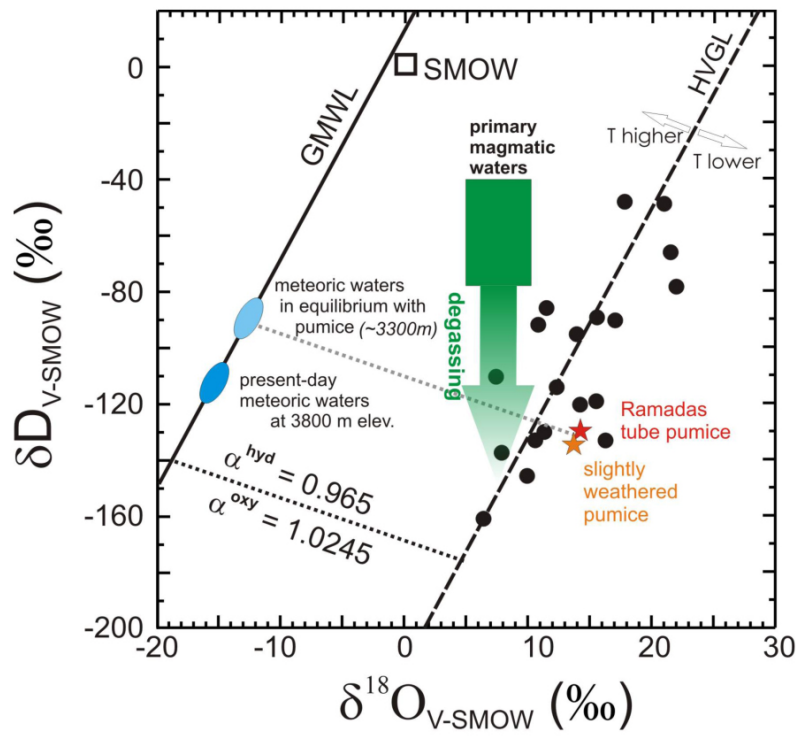


619

620

This page contains no comments

621 Figure 5

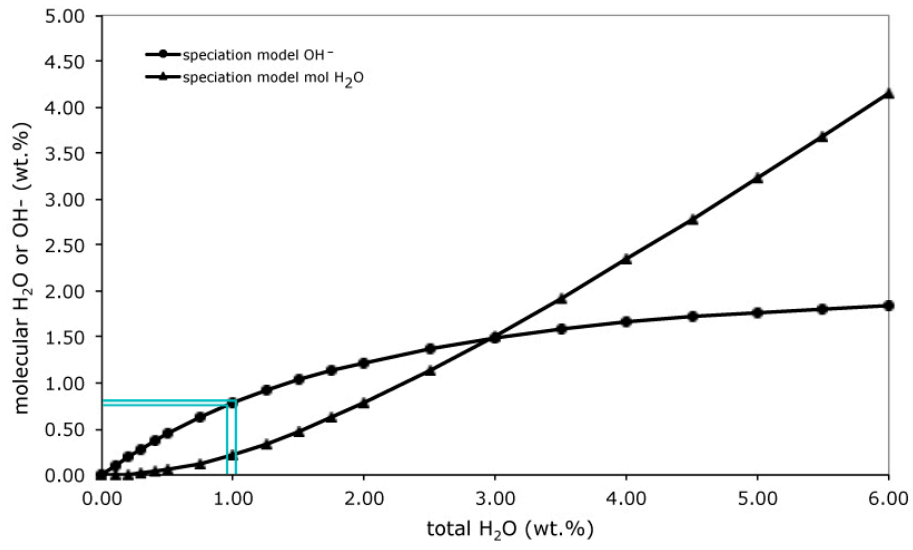


622

623

This page contains no comments

624 Figure 6

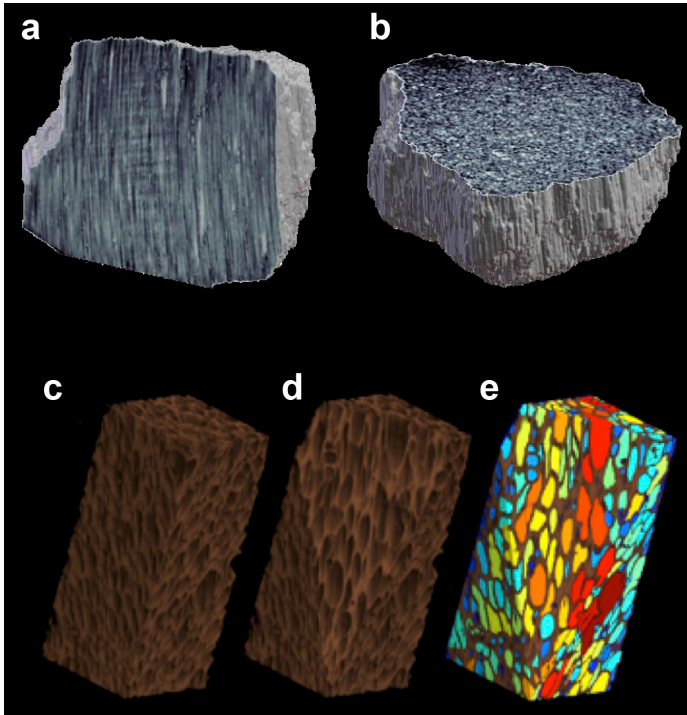


625

626

This page contains no comments

627 Figure 7

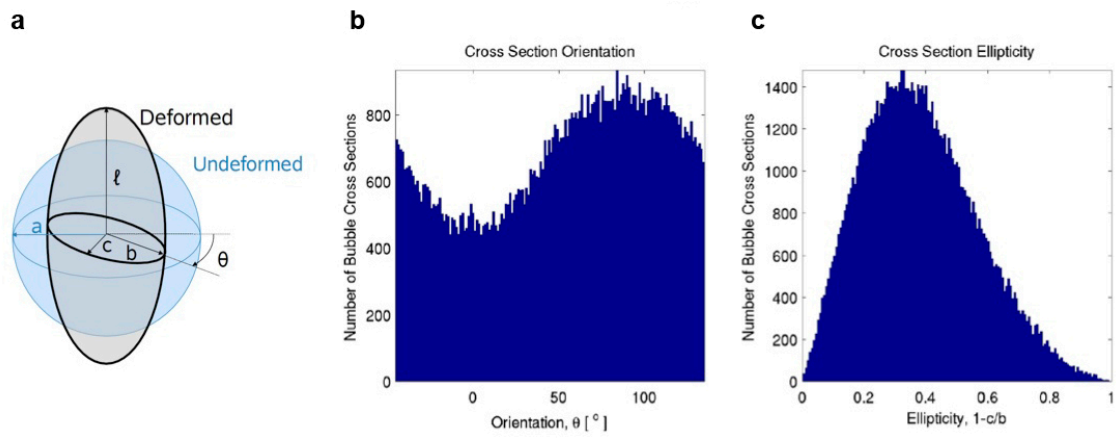


628

629

This page contains no comments

630 Figure 8

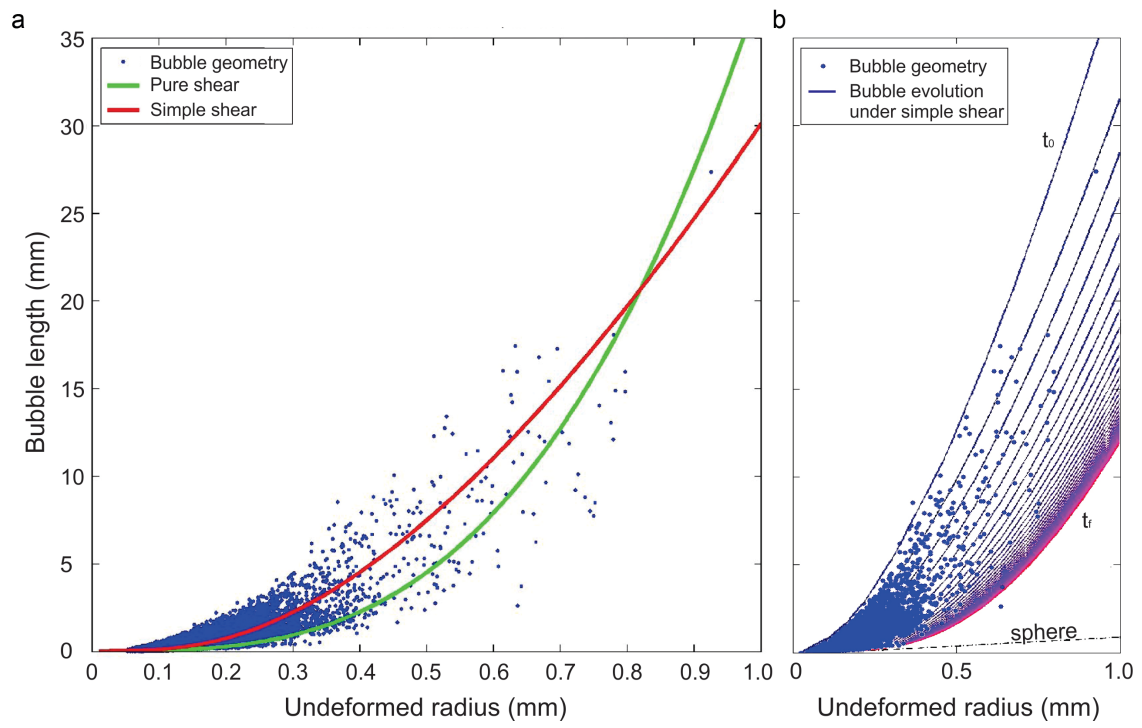


631

632

This page contains no comments

633 Figure 9



634

This page contains no comments